Beam Shaping of VCSEL Arrays Using Randomized Microlens Arrays With Integrated Collimation

Elias Ellingen and Robert Lange

***Abstract*—In active 3D imaging systems, the circular, Gaussian-shaped output of VCSEL arrays must be converted into rectangular patterns aligned with the camera's field of view. To maximize energy efficiency, the beam edges must be sharply confined to avoid illumination outside the target area. For this purpose, this work presents the design, fabrication, and experimental evaluation of randomized microlens arrays (RMLAs) and the novel collimating RMLAs (cRMLAs), which are tailored specifically to the emission characteristics of VCSEL arrays. The freeform optical elements were fabricated using grayscale two-photon polymerization and verified using confocal microscopy. Far-field beam profiles were recorded with a cost-efficient, camera-based setup and analyzed with respect to efficiency, field-of-view coverage, and intensity distribution. The results show that the cRMLAs offer a significant increase in beam shaping efficiency and spatial resolution. This represents the first monolithic randomized microlens array with integrated collimation. The approach enables compact and energy-efficient beam shaping in future active sensing systems.**

***Index Terms*—Beam shaping, microlens arrays, VCSEL arrays, freeform optics, collimating optics, two-photon polymerization.**

I. Introduction

ACTIVE Imaging systems enable precise spatially resolved measurements of several quantities, ranging from multispectral data [1] to distance information [2]. Multispectral imaging is widely used in applications such as forensic science and precision agriculture [3], while accurate distance measurement is essential for industrial safety [4], biometric authentication [5], and self-driving vehicles [6]. The efficiency and robustness of these systems are therefore of great interest to a variety of applications.

Active imaging systems generally consist of an illumination and a receiver subsystem. While receiver subsystems—typically composed of a camera lens and a digital image sensor—are highly optimized, the illumination subsystem still has significant potential for improvement. Many modern active imaging systems utilize arrays of vertical-cavity surface-emitting lasers (VCSELs) as their light source. The emitted light from a VCSEL array must be manipulated to efficiently redirect it into the receiver's field of view (FoV) while imparting a defined irradiance distribution tailored to the imaging technique being used. This challenge is a beam-shaping problem.

Beam shaping is broadly defined by Dickey and Holswade as "the process of redistributing the irradiance and phase of a beam of optical radiation" [7]. A comprehensive overview of beam-shaping techniques for laser beams can be found in [8]. Different beam-shaping methods offer distinct advantages depending on the specific application requirements.

A common approach is to use a single freeform lens that transforms the input beam into a desired output distribution i.e. for reshaping the output of an edge emitting Laser (EEL) [9]. However, this method requires precise knowledge of the input irradiance and wavefront and is therefore only suitable when these parameters are well-defined and stable. This limits its applicability for sources with variable or poorly controlled emission characteristics.

VCSEL arrays can exhibit varying irradiance distributions not only across individual devices but especially between production batches, and since beam shapers for these sources are mass-produced, they should ideally function independently of the incoming irradiance profile. This can be achieved by shaping the beam using a microlens array (MLA). If the irradiance changes slowly enough to be nearly constant across each individual microlens, the output becomes largely independent of the input distribution [10].

Typically, MLAs consist of periodically arranged lenses. However, because VCSELs emit coherent radiation, periodic structures introduce diffraction effects, reducing uniformity and potentially degrading measurement system performance. To mitigate this issue, randomized microlens arrays (RMLAs) are used. Unlike periodic MLAs, RMLAs consist of randomly arranged microlenses, preventing the introduction of periodic diffraction patterns and ensuring a more uniform illumination [10].

The concept of RMLAs was first introduced by Sales et al. in 2002 [11] as a method for homogenizing and shaping laser beams. Later, they expanded on this concept and introduced the term "engineered diffuser" to describe structured microlens arrays optimized for specific beam distributions [12]. Since then, research has focused on improving both fabrication methods—such as wet etching [13], [14] and mask-moving exposure [15]—and design strategies. Liu et al. [16] introduced a geometrical optics-based design method to homogenize uncollimated laser beams, while Song et al. [17] proposed a novel RMLA design enabling large scattering angles (up to $\pm 41^\circ$) through total internal reflection. Their method also introduced an adjustable

Received 29 July 2025; accepted 22 August 2025. Date of publication 28 August 2025; date of current version 9 September 2025. This work was supported in part by the German Federal Ministry of Research, Technology and Space, under Grant 13FH554KX1 and in part by the Institute for Safety and Security Research at the Bonn-Rhein-Sieg University of Applied Sciences. *(Corresponding author: Elias Ellingen.)*

The authors are with the Bonn-Rhein-Sieg University of Applied Sciences, 53757 Sankt Augustin, Germany (e-mail: elias.ellingen@h-brs.de).

Digital Object Identifier 10.1109/JPHOT.2025.3603888

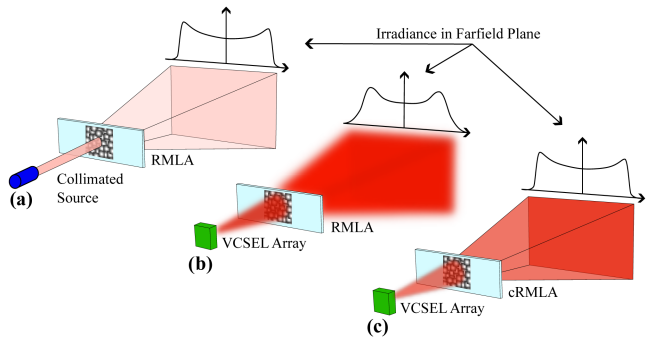

Fig. 1. *Comparison of beam shaping setups using RMLAs and cRMLAs.* (a) A single collimated laser beam illuminates an RMLA, projecting a sharp rectangular batwing profile onto a plane. (b) A VCSEL Array illuminates an RMLA, resulting in a higher power but defocused batwing profile, due to the uncollimated nature of the source. (c) A VCSEL Array illuminates a collimating RMLA, projecting a sharp, high power batwing profile on the plane. The irradiance distributions are schematically shown at the output plane, highlighting the difference in spatial resolution between RMLA and cRMLA.

randomness parameter, balancing uniformity and energy efficiency.

Various methods have been developed for the fabrication of microlens arrays, including inkjet printing, thermal reflow, wet etching, and two-photon polymerization (TPP) [18]. Among these, TPP offers the highest design freedom, enabling the fabrication of freeform and double-sided elements with sub-micron precision [19]. This capability has been exploited in several recent works to fabricate customized micro-optical components, such as phase masks [20], and microlenses for beam shaping and wavefront control [21], [22], printed directly on optical fibers or aspherical air-spaced doublets, printed in a single fabrication step [23]. Building on these advances, this work uses TPP to fabricate collimating randomized microlens arrays (cRMLAs) onto transparent substrates.

This work aims to adapt RMLA designs specifically for VCSEL arrays, fabricate the designed structures using Two-Photon-Polymerization, and evaluate their performance relative to existing commercial solutions. By considering the unique emission characteristics of VCSEL arrays in the design process, we seek to enhance illumination efficiency, ultimately contributing to more precise and energy-efficient active imaging systems.

To this end, we propose a modified beam shaping element—the collimating Random Microlens Array (cRMLA)—a freeform optical element which integrates a collimating surface into the conventional RMLA design. This modification is specifically tailored to counteract the divergence of VCSEL emissions, aiming to maintain the spatial resolution of the shaped beam. This concept is illustrated in Fig. 1.

The remainder of this paper is organized as follows: Section II outlines the design strategy for the cRMLA along with the fabrication process, the verification via confocal microscopy, and the experimental setup for beam profile characterization. Section III presents the results, which are discussed in Section IV. Finally, Section V concludes the paper and provides an outlook on future work.

II. Methods

A. Design and Modeling of Randomized Microlens Arrays

Our design procedure for RMLAs builds on initial work presented in a master's thesis from our research group [24], which itself followed the approach outlined by Sales [10]. While the thesis established the foundational steps, the present work advances the process through more accurate modeling, enhanced fabrication techniques, and an improved beam profile measurement method.

1) Setting of Constraints: Three main constraints need to be set. First, the boundary shape of individual lenses needs to be selected. Generally, it should be equivalent to the shape of the desired field of illumination (FOI) [10]. In this case, a rectangular boundary shape is chosen. Next, the total size of the RMLA needs to be set to include as much of the light emitted by the VCSEL array as possible. The $\frac{1}{e^2}$ divergence of the used VCSEL array is $4.92°$ and the chosen distance between the VCSEL array and RMLA is $10\,\mathrm{mm}$. By setting the RMLA size to $5 \times 5\,\mathrm{mm}^2$ over 99.985% of the total emitted energy reaches the RMLA. Lastly, the size of individual lenses needs to be chosen large enough, such that the lenses work in the refractive regime. At the same time, it should be small, such that a large number of microlenses is illuminated, which increases the uniformity of the output illumination. The minimal lens diameter D can be estimated from the wavelength λ and the beam half-width θ in degrees as $D \geq 1840\frac{\lambda}{\theta}$ [10]. In this work, a lens diameter of $150\,\mu\mathrm{m}$ is chosen. This diameter is about three times larger than the minimum lens diameter calculated for the maximum beam half-width of $30°$ at a wavelength of $940\,\mathrm{nm}$. Further optimization could be achieved by varying this parameter. An increase would improve efficiency at the expense of uniformity, whereas a decrease would enhance uniformity but reduce efficiency [10]. However, such refinements are beyond the scope of this work, which primarily aims to establish the functionality of the cRMLA approach.

2) Design of Individual Microlens: In the second step, a singular microlens is designed, which adheres to the constraints defined in step one. Designing this lens means finding a height profile which produces the desired beam profile under illumination with a plane wave. The assumption of plane wave illumination is based on the idea that individual microlenses are so small that the incoming beam is approximately constant in intensity and phase. To accommodate beam profiles with different FOI sizes along the x and y axis, a biconic surface $h(x, y)$ is chosen, which can be expressed as [25]:

$$h(x,y) = \frac{c_x x^2 + c_y y^2}{1 + \sqrt{1 - (1+k_x)c_x^2 x^2 - (1+k_y)c_y^2 y^2}}, \quad (1)$$

where c_x, c_y and k_x, k_y are the curvature and the conical constant along the respective axes. This approach allows for different curvatures and conical constants in the x and y directions, providing greater flexibility in beam shaping compared to rotationally symmetric surfaces. The optimal lens height profile is then determined by numerically optimizing the parameters

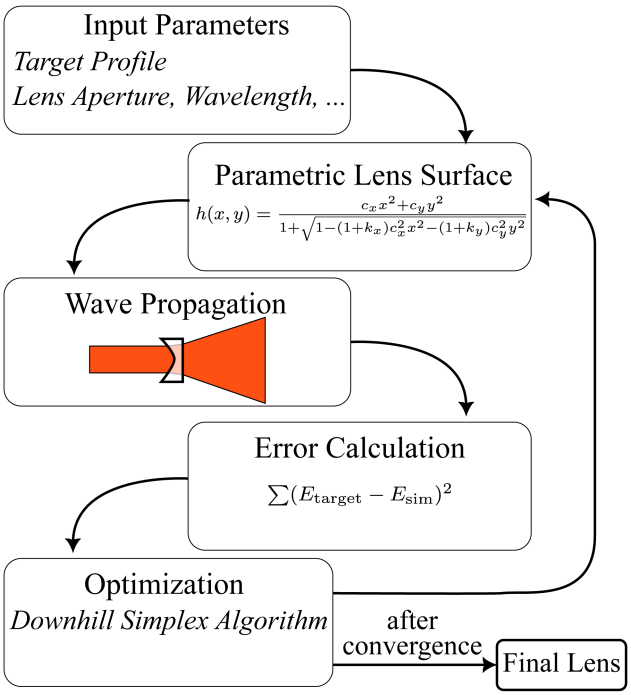

Fig. 2. *Flowchart of the iterative design process for a single microlens.* Starting from a parametric surface, the lens is simulated under collimated illumination. The resulting irradiance distribution is compared with the target, and the design parameters are updated using the downhill simplex algorithm. This process is repeated until the desired beam profile is achieved.

TABLE I
OPTIMIZED MICROLENS PARAMETERS

Parameter	c_x	c_y	K_x	K_y
Value	$15.834\,\text{mm}^{-1}$	$11.230\,\text{mm}^{-1}$	-0.9925	-0.9656

c_x, c_y, k_x, k_y to minimize the squared difference between the target irradiance profile and the simulated profile of a lens with the specified height distribution. This procedure is shown in Fig. 2.

The optimization is performed within the physical optics simulation software *Virtuallabs Fusion*, utilizing a custom detector component to compute the sum of squared differences. The integrated optimization method, based on the downhill simplex method [26], is employed to iteratively refine the lens profile. The refractive index of the IP-S lens material is taken from the datasheet as $\eta = 1.504$ at a wavelength of $940\,\text{nm}$. A more detailed description of the simulation methods can be found at the end of this section.

For the purpose of this work, we design an RMLA with a full width at half max (FWHM) size of $60° \times 45°$, with a batwing profile inside this region defined by the irradiance distribution

$$E(\theta) = \cos^{-2}(\theta) \tag{2}$$

The optimized parameters for a single microlens are shown in Table I.

3) Randomized Placement of Microlenses: The third step is the placement of randomized microlenses. Once the height profile of individual lenses is known, the RMLA surface can be designed by iteratively placing microlenses at random locations within the total area until all points in the area have an associated height [10]. In case a part of the placed microlens overlaps with an existing microlens, the new microlens is ignored in the overlapping region.

To further decrease the periodic nature of the structure, which decreases diffraction artifacts, two other lens parameters are randomized [10]. The first is a random offset d_c of the lens center to the definition area, called decenter. The second is the diameter of each lens D. For each microlens that is placed, the decenter and diameter are drawn from a uniform random distribution. For the diameter, this distribution includes values $D \in [148\,\mu\text{m}, 152\,\mu\text{m}]$. The decenter is defined relative to the chosen diameter D in each iteration as $d_c \in [\frac{-0.1D}{2}, \frac{0.1D}{2}]$ [10]. Optimization of these parameters may improve performance, but is beyond the scope of this work.

4) Optical Modeling of Microlens: The optimization of the single microlens surface requires accurate and fast modeling of the projected irradiance distribution under plane wave illumination. We use the physical optics modeling software *Virtuallabs Fusion* to model the microlens irradiance. The software is configured to first compute the field directly behind the element using the local plane interface approximation (LPIA). This field can then be propagated to the plane at which the irradiance profile is analyzed using a non-paraxial far-field propagation. This method was discussed by Lindlein in 2002 [27] and later expanded on and verified by Shi et al. [28] using finite element method (FEM) solutions of the Maxwell equations as a reference.

The same procedure could in principle be used to model the output of the whole RMLA. However, in practice, the available computing resources are insufficient to sample a $5 \times 5\,\text{mm}^2$ surface with the required sampling distance and compute the output irradiance distribution. Therefore, we rely on the assumption that the total RMLA output should resemble the output of a singular microlens.

B. Adaption to VCSEL Arrays

Although an RMLA can shape the output irradiance distribution independently of the input profile, its performance relies on a collimated input beam. However, VCSEL arrays typically emit uncollimated light. A detailed discussion of uncollimated illumination and different collimation methods can be found in the earlier-cited master's thesis [24].

The impact of using an uncollimated beam for illumination can effectively be analyzed through Fourier optics [29], which relies on the thin element approximation and the Fraunhofer approximation. While these approximations may not be exact in this scenario, they provide useful insight into the effects of uncollimated illumination. If an optical element designed for plane wave illumination is instead illuminated with an uncollimated Gaussian beam, the resulting field in the observation plane will be the original field, convoluted with the Gaussian beam propagated to the same observation plane [30]. Thus, illumination with an uncollimated beam results in a loss of spatial resolution, causing the edges of the field of interest

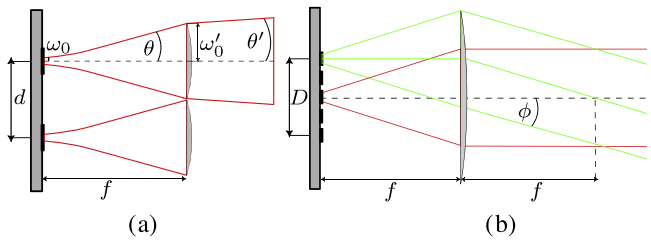

Fig. 3. *Different setups for VCSEL array collimation:* VCSELs can be collimated individually (a). In this case the divergence after collimation is limited by the beam waist, which corresponds to the pitch of the VCSELs d. Alternatively, a single lens can be used to collimate the entire VCSEL array (b). In this case, divergence is governed by the ratio of total array size D and focal length f. [24].

(FOI) to appear more blurred and reducing the efficiency of light utilization.

To combat this effect, the illuminating beams should be collimated. A single Gaussian beam can be collimated using a spherical lens placed one focal length from the beam waist. This approach eliminates wavefront curvature while preserving the beam's amplitude profile [31]. Thus, the beam emerging from the lens propagates as a new Gaussian beam with an increased waist and consequently reduced divergence. The half-angle divergence of the collimated beam in the far field is given by $\theta = \arctan(\frac{\lambda}{\pi\omega_0})$, where ω_0 is the waist radius of the beam behind the lens and λ is the wavelength of the light emitted by the VCSEL [31]. Since a VCSEL array emits an array of multiple Gaussian beams, it is possible to collimate each of the beams with its own lens, as demonstrated in Fig. 3(a). This method has also been reported in previous works [32], [33]. The geometry of this setup should be chosen such that each lens is as large as possible while being illuminated only by one VCSEL. This leads to the largest possible output beam waist ω_0' and the lowest collimated divergence θ'.

The illustration shows that the radius of each lens is half the pitch d between individual VCSELs in the array. The waist radius w_0' of each outgoing beam is equal to the radius of the lens, which leads to the equation $w_0' = \frac{d}{2}$. The resulting divergence θ' can then be calculated as $\theta' = \arctan(\frac{2\lambda}{\pi d})$. The focal length f, which is equal to the distance of the lenses from the VCSEL array, is determined by the VCSEL divergence θ and pitch d as $f = \frac{d}{2\tan(\theta)}$.

The pitch of the used VCSEL array is $50\ \mu\mathrm{m}$, which leads to a beam divergence of $0.69°$ after collimation and a focal length of $f = 290\ \mu\mathrm{m}$. The tight VCSEL pitch and the small focal length will make the alignment of the collimating lens challenging.

Another approach for collimation is to use a single lens placed at a larger distance, which collimates the light emitted by the whole array. Since individual VCSELs are incoherent to each other, they show no interference effects, and the array output can be computed as the sum of all VCSEL intensities. For an infinite distance, the different VCSELs would approximate a point source, and the collimation would be perfect, but in practice, this is not the case. Fig. 3(b) shows the effect the collimating lens has on an off-axis VCSEL. A VCSEL array consisting of five VCSELs with a total size D is shown. The center VCSEL (red) is collimated perfectly, while the off-axis VCSEL (green) is collimated at an angle ϕ. The path of this ray can be constructed by tracing the central ray of the VCSEL, which arrives orthogonal to the lens surface, through the focal spot. Since the beam is collimated by the lens, all other rays emitted by the VCSEL are emitted at the same angle $\phi = \arctan(\frac{D}{2f})$. Thus, the lens creates an image of the VCSEL array focused at infinity. This image consists of collimated points, the furthest of which spread out at angle ϕ.

The used VCSEL array has a total size of $D = 800\ \mu\mathrm{m}$ and is placed at a distance of $f = 10\ \mathrm{mm}$, the maximum divergence is $2.3°$. While the remaining divergence is larger than that for individual collimation, the requirements for alignment are much less strict. Thus, a single collimating lens is chosen for collimation in this work.

To make the optical assembly as compact as possible, the collimating lens is integrated into the RMLA surface. Lee et al. [34] demonstrated that collimation of a diverging light source can be integrated into a diffractive optical element (DOE) by adding the phase shift caused by the collimating lens to the phase shift caused by the DOE, which is equivalent to adding the height of both surfaces.

Analogously, the collimating RMLA (cRMLA) is designed by superimposing the height profile of the collimating lens onto the RMLA profile. In order to reduce the structure height and printing time, a fresnel slicing with a height of $55.95\ \mu\mathrm{m}$ is applied to the combined surface. This approach relies on the thin element approximation (TEA), which neglects refraction effects and remains accurate primarily for small structure heights. However, an analysis of the validity of the TEA or the implementation of a more rigorous strategy for combining the two optical elements is beyond the scope of this work.

The designed height profiles for the RMLA and the cRMLA are shown in Fig. 4. The typical RMLA structure, consisting of multiple randomly arranged microlenses, is visible in Fig. 4(a). Fig. 4(b) shows the cRMLA structure, where the superimposed collimating lens and the Fresnel slicing are visible. The individual microlenses diverge the incoming beam with a negative focal length and a concave surface, whereas the collimating lens has a positive focal length and a convex surface.

C. Fabrication and Verification

The structures were fabricated via grayscale two-photon polymerization using a *Quantum X* system (Nanoscribe GmbH, Germany) equipped with a $25\times$ objective and IP-S photoresist. Superfrost Plus adhesion-coated microscope slides with a thickness of $1\ \mathrm{mm}$ were used as substrates. A full $5 \times 5\ \mathrm{mm}^2$ RMLA can be fabricated in about 30 hours, making the method suitable for rapid prototyping.

Verification of the fabricated microlens profiles was carried out using a confocal microscope (MarSurf CM explorer, NanoFocus AG, Germany). Since the total size of the RMLA significantly exceeds the microscope's field of view, a stitched scan would be required to capture the full structure. However, this approach would be time-consuming and prone to stitching artifacts. Instead, a single microlens within the RMLA was

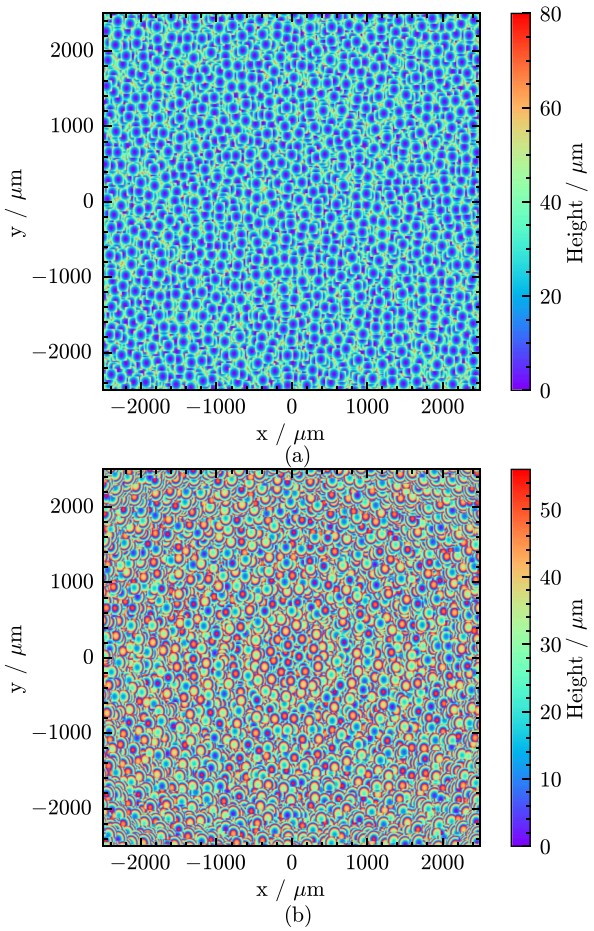

Fig. 4. *Designed height profile for the RMLA and cRMLA:* The designed height profiles for the RMLA (a) and cRMLA (b) are shown as color coded height maps. In the cRMLA structure, the concentric rings caused by the convex collimating lens are visible.

measured. This is justified by the assumption that systematic fabrication errors are similar across all individual microlenses, making a single-element verification sufficient for initial quality control. To ensure there are no errors in the other sections of the surface, the whole element is inspected using a regular microscope with oblique illumination.

Fig. 5 compares the designed and measured microlens profiles for a single microlens and shows an overview of the cRMLA taken with a regular microscope under oblique illumination. The steep edges could not be fully captured due to low reflectivity, but across the measurable area, the root-mean-square (RMS) deviation is $270 \pm 10\,\mathrm{nm}$, indicating good agreement between design and fabrication.

D. Beam Profile Measurement

The beam profile measurement setup ideally captures the irradiance distribution at a plane in the far field. However, for a beam with a diameter of $5\,\mathrm{mm}$ and a wavelength of $0.94\,\mu\mathrm{m}$, the far-field distance, calculated using the antenna designer's formula [29], is approximately $55\,\mathrm{m}$. Such a distance makes a proper far-field measurement highly impractical in a laboratory setting.

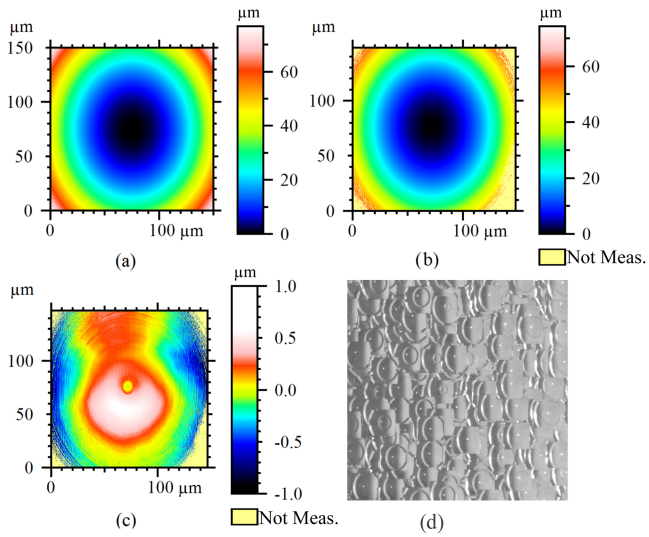

Fig. 5. *Measurements of the fabricated structures* (a) Height-map of a designed microlens; (b) Measured profile of a single mircolens using confocal microscopy; (c) Height difference between design and measurement; (d) Regular microscope image of a part of the cRMLA surface under oblique illumination.

Instead, the measurement distance was chosen based on the target application in a Time-of-Flight (ToF) camera system, where the typical working distance is generally larger than $0.2\,\mathrm{m}$. Consequently, the beam profile was recorded at this minimum distance of $0.2\,\mathrm{m}$. Given that the shaped beam spans an angular extent of approximately $60x45\ \mathrm{deg}$, a direct beam profile measurement at this distance, e.g., using a CMOS beam profiler, is not feasible due to the limited sensor size.

Two viable alternatives for beam characterization remain: goniometric measurements and indirect imaging using a diffusely reflecting or transmitting screen. Due to the limited resolution and extended acquisition times of goniometric methods, an indirect approach based on a transmission screen and a camera was selected.

In this setup, the shaped beam is projected onto a diffusely transmitting screen, which is imaged from the rear side using a 10-bit monochrome CMOS camera equipped with an IR longpass filter. The camera has a resolution of 5536px × 3692px. The measurement setup is illustrated in Fig. 6: A VCSEL array illuminates the beam-shaping component under test, which is mounted on a three-axis translation stage for alignment. The reshaped beam is transmitted through the screen. A lens then images the transmitted light onto the camera sensor.

To account for systematic artifacts in the imaging system, such as lens vignetting or non-uniform scattering of the screen, a calibration was performed using a reference light source with a known irradiance distribution. The resulting reference image is used to compute a pixel-wise correction factor that is applied to all subsequent beam profile images. This calibration step ensures that the measured irradiance distribution accurately reflects the actual irradiance incident on the transmission screen.

The beam shapers are aligned by first placing them at a larger distance from the VCSEL than intended. This way, a portion of the VCSEL beam which does not hit the beam shaper is visible as a bright round spot on the screen. Inside

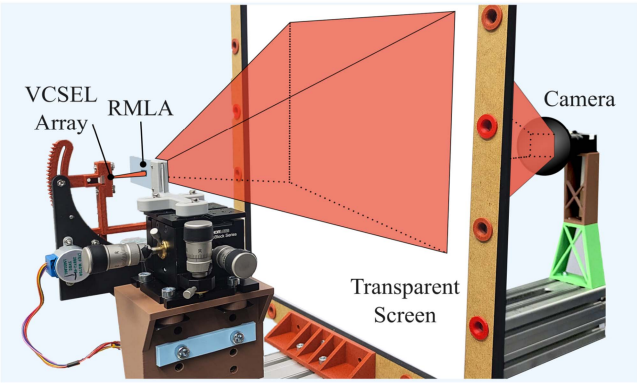

Fig. 6. *Measurement setup for beam profile characterization.* The VCSEL Array illuminates the beam-shaping component under test, and the reshaped beam is transmitted through the beam shaper. A lens then images the transmitted light onto the camera sensor.

this spot, the rectangular shadow of the beam shaper is visible and can be used for alignment orthogonal to the optical axis. Then the beam shaper is moved to the desired distance of $10\,\mathrm{mm}$.

To quantitatively characterize the beam profiles, a set of metrics was defined and extracted from the measurements:

- *Field of Illumination (FOI):* The angular extent of the illumination is quantified using the full width at half maximum (FWHM). The FWHM is determined independently for the horizontal and vertical directions by evaluating intensity profiles extracted along the corresponding axes.
- *Edge Width:* To assess the sharpness of the beam boundary, the edge width is defined as the angular distance between 20% and 80% of the peak intensity along each axis. A smaller edge width indicates a sharper beam transition and better confinement of the illumination.
- *Batwing Profile Strength:* To quantify the characteristic batwing shape of the irradiance distribution $E(\theta)$, the light in the FOI is fitted with the function $E(\theta) = cos(\theta)^{-n}$. The fitted exponent n serves as a measure of the peripheral intensity: higher values indicate a stronger batwing profile with more pronounced edge illumination.
- *Beam Shaping Efficiency:* This metric captures how effectively the beam shaper concentrates light into the desired angular region. It is defined as the ratio of the optical power within the measured FOI to the total transmitted power through the optical component.
- *Transmission Efficiency:* The absolute transmission efficiency of each beam shaper is determined via a separate measurement using an integrating sphere. This measurement quantifies the fraction of the incident optical power that is transmitted through the beam shaper.
- *Total Efficiency:* This final metric combines beam shaping and transmission performance. It is defined as the ratio of optical power within the FOI to the total power emitted by the VCSEL source. It is calculated as the product of the beam shaping efficiency and the transmission efficiency.

TABLE II
MEASURED METRICS

Metric	Commercial RMLA	RMLA	cRMLA
FWHM (Target $60° \times 45°$)	$57.6° \times 46.6°$	$58.1° \times 43.92°$	$56.7° \times 42.9°$
Edge Width (x,y)	7.9°, 9.3°	8.6°, 9.2°	4.8°, 5.0°
Batwing Strength (Specified)	3.0	0.6 (2)	-2.1 (2)
Beam-Shaping Efficiency	75.5 %	75.2 %	79.8 %
Transmission Efficiency	94.3 %	94.6 %	90.2 %
Total Efficiency	71.2 %	71.4 %	72.0 %

III. RESULTS

Beam profiles, total transmitted power, and derived performance metrics were evaluated for three beam-shaping configurations: a commercial VCSEL array with an integrated randomized microlens array (RMLA), the same VCSEL array combined with a self-fabricated RMLA, and the array with a self-fabricated collimating RMLA (cRMLA).

Table II summarizes the key quantitative performance metrics for all three beam shaping configurations. The corresponding measured irradiance distributions and their horizontal and vertical line profiles are presented in Fig. 7, with green rectangles indicating the target field of view (FOV) of $60° \times 45°$. For comparability, all datasets are normalized such that the total irradiance is equal across all measurements. Since the cRMLA concentrates the available illumination on the smallest area, it appears the brightest.

The measured FOIs for all beam-shaping configurations match the respective design specifications, indicating both the functional accuracy of the fabricated elements and the reliability of the measurement setup. In terms of transmission efficiency, the self-fabricated RMLA achieves $94.6\,\%$, closely matching the commercial reference at $94.3\,\%$. The cRMLA exhibits a slightly lower transmission efficiency of $90.2\,\%$.

The beam-shaping efficiency, defined as the ratio of transmitted power directed into the desired FOI, is comparable between the commercial RMLA ($75.5\,\%$) and the self-fabricated RMLA ($75.2\,\%$). The cRMLA outperforms both with a higher beam-shaping efficiency of $79.8\,\%$.

Edge sharpness, characterized by the spatial width over which the irradiance transitions from 80% to 20% of its peak value, is significantly improved in the cRMLA configuration. The edge width is reduced by up to 48% compared to the other two setups. The measured batwing strength was 0.6 for the self-fabricated RMLA, compared to the design value of 2. The cRMLA exhibited an even lower batwing strength of –2.1. A lower batwing strength indicates an over-concentration of light in the center of the FOI.

IV. DISCUSSION

The measured performance confirms the functional validity of both self-fabricated optical elements. The high transmission

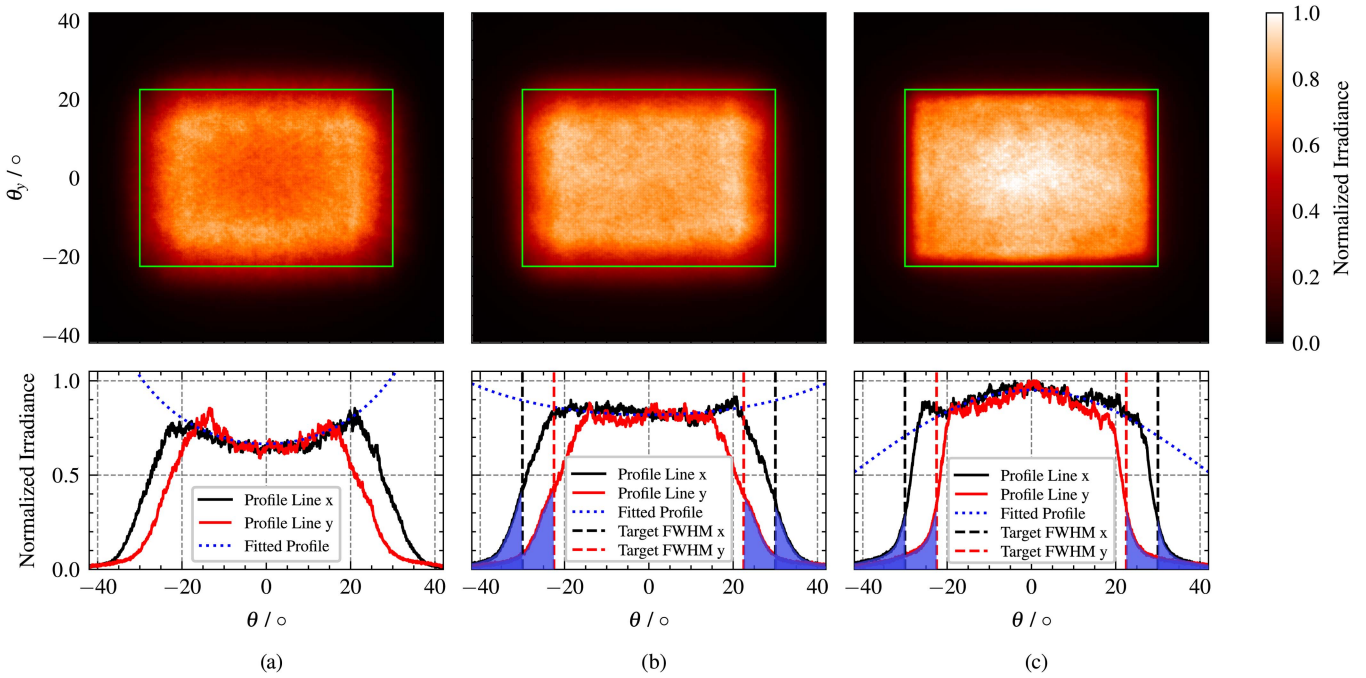

Fig. 7. *Measured beam profiles and line cuts.* Measured irradiance distributions are shown for (a) the commercial RMLA, (b) the self-fabricated RMLA, and (c) the self-fabricated cRMLA, along with corresponding irradiance profiles along the x and y axes. Green rectangles indicate the specified field of illumination (FOI) in the images. For the line cuts of the self-fabricated beam shapers, dashed vertical lines denote the designed FWHM. Blue dotted lines indicate the fitted batwing profile. Blue shaded areas indicate energy falling outside the desired FOI. Comparison of the images as well as the blue shaded areas shows a clear reduction of light lost outside the FOI for the cRMLA (c).

efficiency observed for the self-fabricated RMLA indicates minimal optical losses and confirms that the fabrication process yields surfaces with low scattering and absorption. The slightly reduced efficiency of the cRMLA can be attributed to additional reflection and potential shadowing effects introduced by the collimating surface.

The cRMLA's higher beam-shaping efficiency and sharper edge transitions suggest that the integrated collimation effectively reduces angular spread and enhances light concentration within the desired FOV. These characteristics are consistent with the intended function of the cRMLA and are visibly confirmed in the irradiance maps in Fig. 7.

The discrepancy between the measured and designed batwing strengths for both self-fabricated optics warrants further analysis. The reduced batwing strength may result from fabrication inaccuracies, particularly in the steep outer zones of the microlenses that are critical for generating peripheral rays. Confocal surface measurements did not provide valid measurements in these regions, potentially leading to undetected deviations in lens shape.

In the cRMLA, the negative batwing strength suggests an even stronger concentration of light near the optical axis. This could stem from Fresnel slicing effects at the collimating surface, causing partial occlusion of high-angle rays. Additionally, the steeper curvature in the outer regions of the collimating lens may lead to increased Fresnel reflection, selectively reducing transmission in those zones most responsible for peripheral illumination.

Despite calibration of the measurement system for vignetting and screen scattering, residual systematic errors may still influence the beam profile measurements. Independent verification using a goniometric setup could verify the measured intensity distribution and support further optimization of the beam shaping design.

In practice, the batwing strength and FOI of the cRMLA can also be optimized through iterative design, leveraging the rapid prototyping capabilities of two-photon polymerization (TPP) printing. This enables fast turnaround cycles between simulation, fabrication, and measurement, allowing systematic refinement of the microlens geometry to achieve the desired angular intensity distribution.

These results show that integrating a collimating surface into a microlens array can enhance beam-shaping efficiency and angular resolution, confirming the viability of this approach for compact, high-performance illumination systems.

V. Conclusion

The results confirm that the proposed design strategy for adapting Random Microlens Arrays (RMLAs) to the emission characteristics of VCSEL arrays is viable. Both self-fabricated beam shapers achieved beam profiles and fields of view close to their design specifications, demonstrating the validity of the design procedure as well as the effectiveness of the grayscale two-photon polymerization process for fabricating complex freeform micro-optics.

A key novelty of this work is the fabrication and optical characterization of a cRMLA — a Random Microlens Array with an integrated collimating surface — realized as a single, monolithic optical component. This is the first reported instance

of such an element being proposed and experimentally verified. The far-field beam profiles were measured using a cost-efficient, camera-based setup. Among all tested beam shapers, the cRMLA achieved the highest beam shaping and overall efficiency, highlighting the potential of this integrated design approach for compact and energy-efficient illumination systems.

While the measured batwing profile strength was lower than designed for the self-fabricated RMLAs and further reduced in the cRMLA, two likely causes for this effect have been identified and can be addressed in future design iterations. Despite the reduced batwing strength, the cRMLA delivers more light into the outermost regions of the FOI than the RMLA due to its narrower edge width. In the context of active imaging systems, this improved edge illumination will enhance measurement robustness near the boundaries of the field of view, even with a less pronounced batwing profile.

To further enhance performance, future work can explore the following directions:

- Application of anti-reflection coatings to reduce Fresnel losses and improve overall efficiency.
- Joint optimization of the collimating and beam-shaping surfaces to preserve the desired angular intensity distribution.
- Further validation of the camera-based measurement method using goniometric measurements.
- Extension of the integrated collimation approach to computer-generated holograms (CGHs) for structured illumination.
- Investigation of improved Fresnel slicing strategies or alternative lens geometries to mitigate internal shading and improve edge illumination.

In summary, this work demonstrates a promising new class of monolithic beam shaping optics that combine beam shaping and collimation in a single optical element. The concept is shown to be feasible and effective, with strong potential for further optimization and extension to other application domains in active optical systems.

Acknowledgment

The authors would like to thank the Smart Photonic Systems (IPS) workgroup for their support throughout this research. Special thanks go to Titus Lange for his contributions to the beam profile measurement setup.

The authors acknowledge the use of AI-based tools, like ChatGPT, for assistance with editing, grammar enhancement, and spelling checks during the preparation of this manuscript.

Code and Data Availability

All code and data necessary to reproduce these results are available from the authors upon request.

References

[1] U. Simoncic and M. Milanic, "Hyperspectral imaging with active illumination: A theoretical study on the use of incandescent lamp and variable filament temperature," *Sensors (Basel, Switzerland)*, vol. 23, no. 23, Nov. 2023, Art. no. 9326. [Online]. Available: https://www.ncbi.nlm.nih.gov/pmc/articles/PMC10708585/

[2] M.-A. Drouin and J.-A. Beraldin, "Active 3D Imaging Systems," in *3D Imaging, Analysis and Applications*, N. Pears, Y. Liu, and P. Bunting, Eds. London, U.K.: Springer, 2012, pp. 95–138, doi: 10.1007/978-1-4471-4063-4_3.

[3] M. J. Khan, H. S. Khan, A. Yousaf, K. Khurshid, and A. Abbas, "Modern trends in hyperspectral image analysis: A review," *IEEE Access*, vol. 6, pp. 14118–14129, 2018. [Online]. Available: https://ieeexplore.ieee.org/document/8314827

[4] P. Rybski, P. Anderson-Sprecher, D. Huber, C. Niessl, and R. Simmons, "Sensor fusion for human safety in industrial workcells," in *Proc. 2012 IEEE/RSJ Int. Conf. Intell. Robots Syst.*, 2012, pp. 3612–3619.

[5] N. Pears and A. Mian, *3D Face Recognition*. Cham, Switzerland: Springer, 2020, pp. 569–630, doi: 10.1007/978-3-030-44070-1_12.

[6] C. Badue et al., "Self-driving cars: A survey," *Expert Syst. Appl.*, vol. 165, 2021, Art. no. 113816. [Online]. Available: https://www.sciencedirect.com/science/article/pii/S095741742030628X

[7] F. M. Dickey and S. C. Holswade, "Beam shaping a review," in *Laser Beam Shaping Applications*, F. M. Dickey and T. E. Lizotte, Eds. Boca Raton, FL, USA: CRC Press, Feb. 2017, pp. 329–356.

[8] F. M. Dickey, Ed., *Laser Beam Shaping: Theory and Techniques*. Boca Raton, FL, USA: CRC Press, 2014.

[9] F. Shen et al., "Tailoring freeform beam-shaping lenses for edge-emitting lasers," *Opt. Lasers Eng.*, vol. 167, 2023, Art. no. 107603. [Online]. Available: https://www.sciencedirect.com/science/article/pii/S014381662300132X

[10] T. R. Sales, "Engineered microlens diffusers," in *Laser Beam Shaping: Theory and Techniques*, F. M. Dickey, Ed. Boca Raton, FL, USA: CRC Press, 2014, vol. 9, pp. 367–439.

[11] T. R. Sales, G. Gretton, G. M. Morris, and D. H. Raguin, "Beam shaping and homogenization with random microlens arrays," presented at the Diffractive Opt. Micro-Optics, Tucson, AZ, USA, Jun. 3–6, 2002, Paper DMA3. [Online]. Available: https://opg.optica.org/abstract.cfm?URI=DOMO-2002-DMA3

[12] T. R. Sales, "Bandlimited illumination with engineered diffusers," *Adv. Opt. Technol.*, vol. 1, no. 3, pp. 127–134, 2012, doi: 10.1515/aot-2012-0012.

[13] L. Xue et al., "Fabrication of random microlens array for laser beam homogenization with high efficiency," *Micromachines*, vol. 11, no. 3, 2020, Art. no. 338. [Online]. Available: https://www.mdpi.com/2072-666X/11/3/338

[14] H. Zhang et al., "Random silica-glass microlens arrays based on the molding technology of photocurable nanocomposites," *ACS Appl. Mater. Interfaces*, vol. 15, no. 15, pp. 19230–19240, 2023, doi: 10.1021/acsami.3c02040.

[15] W. Yuan, L. Xue, A. Cao, H. Pang, and Q. Deng, "Close packed random rectangular microlens array used for laser beam homogenization," *Opt. Exp.*, vol. 29, no. 25, pp. 40878–40890, Dec. 2021. [Online]. Available: https://opg.optica.org/oe/abstract.cfm?URI=oe-29-25-40878

[16] Z. Liu, H. Liu, Z. Lu, Q. Li, and J. Li, "A beam homogenizer for digital micromirror device lithography system based on random freeform microlenses," *Opt. Commun.*, vol. 443, pp. 211–215, 2019. [Online]. Available: https://www.sciencedirect.com/science/article/pii/S0030401819302524

[17] H. Song et al., "Design of random microlens arrays with large scattering angles," *Opt. Laser Technol.*, vol. 182, 2025, Art. no. 112176. [Online]. Available: https://www.sciencedirect.com/science/article/pii/S0030399224016347

[18] S. Cai, Y. Sun, H. Chu, W. Yang, H. Yu, and L. Liu, "Microlenses arrays: Fabrication, materials, and applications," *Microsc. Res. Technique*, vol. 84, no. 11, pp. 2784–2806, 2021. [Online]. Available: https://analyticalsciencejournals.onlinelibrary.wiley.com/doi/abs/10.1002/jemt.23818

[19] D. Gonzalez-Hernandez, S. Varapnickas, A. Bertoncini, C. Liberale, and M. Malinauskas, "Micro-optics 3D printed via multi-photon laser lithography," *Adv. Opt. Mater.*, vol. 11, no. 1, 2023, Art. no. 2201701. [Online]. Available: https://advanced.onlinelibrary.wiley.com/doi/abs/10.1002/adom.202201701

[20] T. Gissibl, M. Schmid, and H. Giessen, "Spatial beam intensity shaping using phase masks on single-mode optical fibers fabricated by femtosecond direct laser writing," *Optica*, vol. 3, no. 4, pp. 448–451, Apr. 2016. [Online]. Available: https://opg.optica.org/optica/abstract.cfm?URI=optica-3-4-448

[21] Z. Li et al., "Doughnut beam shaping based on a 3D nanoprinted microlens on fiber tip," *Opt. I Laser Technol.*, vol. 167, 2023, Art. no. 109798. [Online]. Available: https://www.sciencedirect.com/science/article/pii/S0030399223006916

[22] C. Su et al., "Spatial beam intensity shaping based on an on-fiber 3D nanoprinted microlens," *J. Lightw. Technol.*, vol. 43, no. 8, pp. 3968–3973, 2025.

[23] L. Siegle, S. Ristok, and H. Giessen, "Complex aspherical singlet and doublet microoptics by grayscale 3D printing," *Opt. Exp.*, vol. 31, no. 3, pp. 4179–4189, Jan. 2023. [Online]. Available: https://opg.optica.org/oe/abstract.cfm?URI=oe-31-3-4179

[24] E. Ellingen, "Design, fabrication and verification of microoptics for illumination beamshaping in active imaging systems," M. S. Thesis, Hochschule Bonn-Rhein-Sieg, Rheinbach, Germany, 2024.

[25] S. Wang, Q. Zhao, Y. Pan, and B. Guo, "Ultra-precision raster grinding biconical optics with a novel profile error compensation technique based on on-machine measurement and wavelet decomposition," *J. Manuf. Processes*, vol. 67, pp. 128–140, 2021. [Online]. Available: https://www.sciencedirect.com/science/article/pii/S1526612521003066

[26] J. A. Nelder and R. Mead, "A simplex method for function minimization," *Comput. J.*, vol. 7, no. 4, pp. 308–313, Jan. 1965, doi: 10.1093/comjnl/7.4.308.

[27] N. Lindlein, "Simulation of micro-optical systems including microlens arrays," *J. Opt. A: Pure Appl. Opt*, vol. 4, no. 4, pp. S1–S9.

[28] R. Shi, C. Hellmann, and F. Wyrowski, "Physical-optics propagation through curved surfaces," *J. Opt. Soc. Amer. A*, vol. 36, Jun. 2019, Art. no. 1252.

[29] J. W. Goodman, *Introduction to Fourier Optics*, 3 rd ed. New York, NY, USA: W. H. Freeman, Jan. 2005.

[30] B. C. Kress and P. Meyrueis, *Digital Optics Modeling Techniques*. Hoboken, NJ, USA: Wiley, 2009, pp. 47–69, ch. 11.

[31] O. Svelto, *Principles of Lasers*. New York, NY, USA: Springer, 2010. [Online]. Available: https://books.google.de/books?id=ioywRI5W2HEC

[32] B. C. Kress and P. Meyrueis, *Refractive Micro-Optics*. Hoboken, NJ, USA:Wiley, 2009, pp. 47–69,ch. 4.

[33] Z. Wang et al., "High power and good beam quality of two-dimensional VCSEL array with integrated gaas microlens array," *Opt. Exp.*, vol. 18, no. 23, pp. 23900–23905, Nov. 2010.

[34] J. Lee, J. Hahn, and H. Kim, "Diffractive optical element for noise-reduced beam shaping of multi-array point light source," *Curr. Opt. Photon.*, vol. 5, no. 5, pp. 506–513, Oct. 2021. [Online]. Available: https://opg.optica.org/copp/abstract.cfm?URI=copp-5-5-506